Journal of Renewable Materials

Tech Science Press

Doi:10.32604/jrm.2025.02025-0004

ARTICLE

# Impact of Pyrolysis Parameters on Biochar and Activated Carbon Properties from *Cistus ladaniferus* for Environmental Applications

**Hammadi El Farissi[1,2,*], Anass Choukoud[1,2], Bouchaib Manoun[3,4], Mohamed El Massaoudi[5,6] and Abdelmonaem Talhaoui[2]**

[1]Chemical Engineering for Resources Valorization Group (UAE/L01FST), Faculty of Science and Technology, Abdelmalek Essaadi University, Tangier, 90002, Morocco

[2]Laboratory of Environment and Applied Chemistry, Team: Physical Chemistry of the Natural Resources and Processes, Faculty of Sciences, Mohammed First University, Oujda, 60000, Morocco

[3]Materials Science and Nano Engineering Department, Mohammed VI Polytechnic University, Ben Guerir, 43150, Morocco

[4]Radiation-Matter and Instrumentation Laboratory, Faculty of Sciences and Technology (FST), Hassan First University, Settat, 926000, Morocco

[5]Laboratory of Applied Chemistry and Environment, Faculty of Sciences, University Mohammed the First, MB 524, Oujda, 60000, Morocco

[6]Higher School of Education and Training, Mohammed First University, Oujda, 60000, Morocco

*Corresponding Author: Hammadi El Farissi. Email: hammadielfarissi04@gmail.com

Received: 04 January 2025; Accepted: 27 March 2025; Published: 23 June 2025

**ABSTRACT:** In light of the growing urgency to address environmental degradation and improve carbon sequestration strategies, this study rigorously investigates the potential of *Cistus ladaniferus* as a viable feedstock for biochar and activated carbon production. The influence of pyrolysis temperature, heating rate and particle size on biochar yield was systematically examined. The results demonstrate that increasing pyrolysis temperature and heating rate significantly reduces biochar yield, while particle size plays a crucial role in thermal degradation and biochar retention. To evaluate the structural and chemical properties of the materials, various characterization techniques were employed, including Fourier-transform infrared spectroscopy (FTIR), scanning electron microscopy (SEM), and energy-dispersive X-ray analysis (EDXA). FTIR identified key functional groups, while SEM and EDXA provided valuable insights into the morphology and elemental composition of the materials. Activated carbons exhibited enhanced porosity and carbon content compared to their biochar counterparts, achieving specific surface areas of up to 1210 $m^2$ $g^{-1}$ for acid-activated shells (AC-Sha). The Brunauer-Emmett-Teller (BET) method confirmed the mesoporous characteristics of these materials, with AC-Sa displaying a surface area of 678.74 $m^2$ $g^{-1}$ and an average pore size of 2.73 nm. Elemental analysis revealed that activated carbons possessed a higher carbon content (96.40 wt.% for AC-Sha) and lower oxygen content (2.37 wt.%), highlighting their suitability for applications in adsorption and catalysis. These findings underscore the significant impact of activation processes on the stability and adsorption capabilities of Cistus-derived biochars and activated carbons, paving the way for future research and practical applications in pollution control, carbon sequestration, and bioenergy.

**KEYWORDS:** Biomass conversion; thermal process; heating rate; shells; seeds; BET; adsorption; eco-friendly

## 1 Introduction

Climate change is one of the most pressing challenges of the 21st century, characterized by a rise in the global average temperature of approximately 1.1°C since the pre-industrial era [1]. According to the

Intergovernmental Panel on Climate Change (IPCC), climate change is driving extreme weather events, ocean acidification, and significant biodiversity loss [2]. These findings are detailed in the IPCC's the Sixth Assessment Report: *Climate Change 2022: Impacts, Adaptation, and Vulnerability*, a contribution of Working Group II [3,4]. In this context, it is increasingly imperative to develop innovative and sustainable strategies to mitigate these impacts, particularly through the adoption of technologies that promote carbon sequestration and enhance the resilience of ecosystems [5].

Biochar, a carbonaceous material produced through the pyrolysis of biomass, offers a promising solution in this fight against climate change [6]. This thermal process, conducted in the absence of oxygen, converts biomass into a stable product that can be integrated into the soil to enhance its structure, fertility and water retention capacity. Moreover, biochar plays a pivotal role in pollutant adsorption and long-term carbon sequestration, contributing to the reduction of atmospheric carbon dioxide concentrations [7]. The performance and properties of biochar are highly influenced by the type of biomass used and the specific conditions of the pyrolysis [8].

Agricultural residues, such as seeds and shells [9], represent a sustainable and perennial source for biochar production. Among these resources, *Cistus ladaniferus*, a widely distributed Mediterranean shrub, remains underexploited despite its considerable potential. Adapted to diverse environmental conditions and highly resistant to drought, this species produces biomass rich in organic compounds, making it an excellent candidate for thermochemical valorization [10]. However, the growing interest in biochar is not without its challenges. Most research focused on conventional biomass, such as wood residues and common agricultural by-products [11], while the potential of alternative sources, including essential oil residues derived from *Cistus ladaniferus*, remains largely unexplored [12]. Gaining a comprehensive understanding of the specific properties of biochar produced from this biomass is crucial to optimize its applications and enhance its effectiveness across various ecological contexts [13].

This work proposes an innovative approach involving the pyrolysing of the seeds and shells of *Cistus ladaniferus* to produce biochar. By leveraging the plant's high biomass yield, the process optimizes pyrolysis conditions to enhance biochar quality. This strategy not only minimizes waste, but also supports sustainable development while contributing to environmental improvement. *Cistus ladaniferus* was selected due to its abundant presence in Mediterranean regions, making it an ideal candidate for energy production and environmental applications. This research proposes a sustainable strategy for utilizing local resources, reducing waste and creating advanced materials for the environment and agriculture applications. Biochar was produced under controlled pyrolysis conditions: the seeds were heated at a temperature ramp rate of 21°C $min^{-1}$ with particle sizes ranging from 0.3 to 0.6 mm, while the shells were heated at a ramp rate of 40°C $min^{-1}$ with particle sizes of 2 to 3 mm, both at a final temperature of 450°C. Following synthesis, the biochar was chemically activated using $H_3PO_4$ (phosphoric acid) and NaOH (sodium hydroxide). A series of characterization techniques were subsequently employed to evaluate the properties of the activated biochar.

## 2 Materials and Methods

### *2.1 Biomass*

The experimental campaigns utilized two types of biomasses from *Cistus ladaniferus*: seeds and shells, characterized by low and high ash content, respectively. These biomasses were collected from the Tangier-Tetouan-Al Hoceïma region, specifically the Al Hoceïma province (Targuist-Bani Hadifa) and the Rmilatte forest in Tangier. After collection, the samples were sun-dried for two weeks, and subsequently shade dried for one month. They were then crushed and stored in airtight plastic containers.

### 2.2 Experimental Procedure

Experiments were conducted to study the influence of pyrolysis temperature (200°C–550°C) at heating rates ranging from 7 to 28°C $min^{-1}$ for seeds and from 10 to 70°C $min^{-1}$ for shells. The experiments utilized a cylindrical semi-batch reactor made of stainless steel, which was vertically inserted into an electrically heated furnace (Fig. 1). The reactor temperature was controlled using a PID controller. During the pyrolysis process, the biomass sample (*Cistus ladaniferus* seeds or shells) was introduced into the reactor. Vapors generated during pyrolysis were directed to a condenser cooled with chilled water to collect the liquid condensate. After each experiment, the condensed liquid was collected in a cylindrical measuring device. The solid residue (charcoal) remaining after pyrolysis was removed, weighed, and analyzed. The biomass feedstock and the resulting charcoal were weighed using an electronic balance with an accuracy of ±0.01 g. Fig. 1 provides a detailed illustration of the experimental setup.

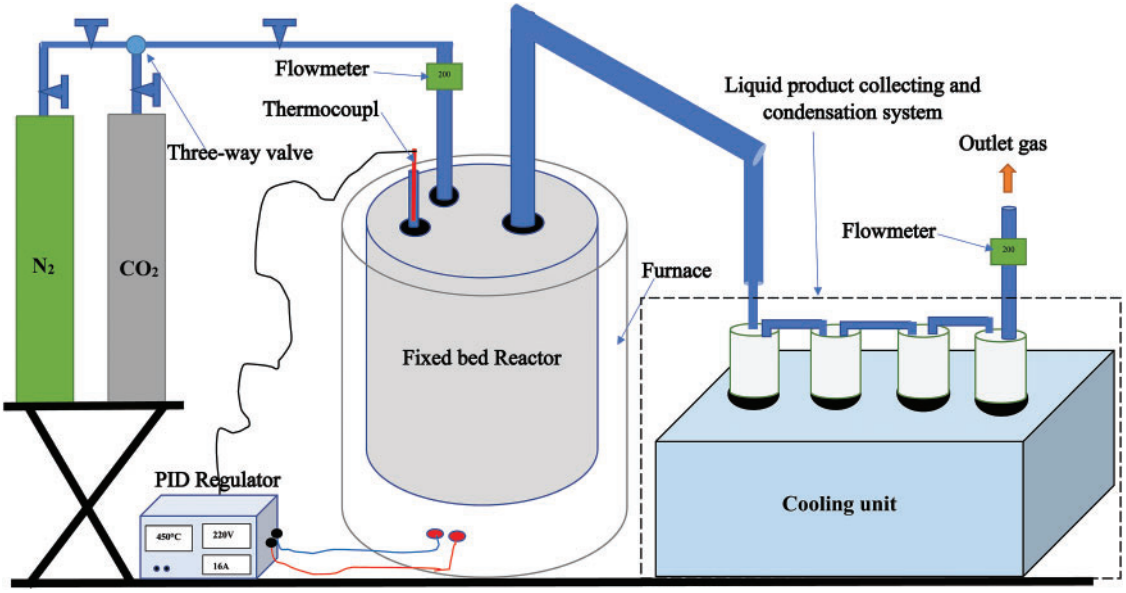


**Figure 1:** Experimental pyrolysis setup

### 2.3 Biochar Activation

#### 2.3.1 Activation with Phosphoric Acid $H_3PO_4$

Phosphoric acid ($H_3PO_4$) is one of the most commonly used agents for the activation of biochar [14,15]. In this process, *Cistus ladaniferus* shells (ACSh) is treated with a solution of $H_3PO_4$ (≥85% purity) at weight ratio of 1:1. The impregnated mixture is then heated in an oven at 100°C for 24 h. Following activation, the acid-treated shells (ACSha) are thoroughly rinsed with distilled water to remove impurities. A subsequent neutralization step is carried out using a 2 M sodium bicarbonate ($NaHCO_3$) solution to eliminate residual acidity. The ACSha is then washed repeatedly with distilled water until the pH of the wash water stabilizes at 6. Finally, the samples are dried at 100°C. This same procedure is also used to activate biochar derived from seeds.

#### 2.3.2 Activation with Sodium Hydroxide (NaOH)

Sodium hydroxide (NaOH) is widely recognized as an effective biochar activation agent in the literature. In this method, 10 g of *Cistus ladaniferus* shells charcoal (ACSh) is initially treated with a 97% sulfuric acid

($H_2SO_4$) solution. The acid, acting as a desiccant, oxidizing agent, and mineral removing agent, is left to soak the charcoal for 24 h. After the soaking process, the ACSh is thoroughly rinsed with distilled water until the pH of the wash water stabilizes at 6. The pretreated charcoal is first immersed in 200 mL of a 4 M NaOH solution and stirred at 85°C for 2 h. The mixture is then filtered, and the NaOH-activated shell powder (ACShb), is dried at 120°C for 24 h. This procedure is similarly applied to activate biochar derived from seeds.

### *2.4 Caracterisation of Biochar and Activated Charcoal*

To analyze the physicochemical properties of biochar and activated carbon, several advanced characterization techniques were employed, each paired with specialized instrumentation. Fourier transform infrared spectroscopy (FTIR), performed using a JASCO 4700 FTIR spectrometer, identified functional groups on the sample surfaces, providing key insights into their chemical composition. Scanning electron microscopy (SEM) coupled with energy-dispersive X-ray analysis (EDXA), conducted using a Hirox-SH-5500P instrument, revealed details about the morphology, including surface features and porosity. The textural properties of the adsorbent were characterized using nitrogen sorption analysis at 77.3 K with a Micromeritics ASAP 2420 analyzer. Prior to analysis, the samples were degassed for 5 h at the same temperature to remove surface contaminants. The specific surface area was determined using the BET (Brunauer-Emmet-Teller) method [16,17], while pore size and volume calculations were performed using the BJH (Barrett-Joyner-Halenda) approach, based on the desorption branch of the isotherm [18]. X-ray diffraction (XRD), carried out with an XDR 6000 instrument, was used to identify the crystalline phases within the samples. Collectively, these techniques and their respective instruments, provided a comprehensive understanding of the properties of biochar and activated carbon, which is crucial for applications in pollution control and carbon sequestration.

### *2.5 Adsorption Process*

To determine The study aimed to determine the adsorption parameters, constants, isotherms, and kinetics of amoxicillin and metronidazole on activated carbon. The process began with the preparation of a calibration curve, using seven solutions with concentrations ranging from 10 to 70 mg $L^{-1}$. Absorbance measurements were conducted with a JASCO V-730 spectrophotometer to ensure accuracy. For the adsorption kinetics analysis, the contact time between the adsorbent and the adsorbates was varied from 20 to 160 min. The solutions were stirred at a constant speed of 150 rpm, followed by centrifugation at 3000 rpm for 2 min. To study the adsorption isotherms, the concentration of the antibiotic solutions was varied between 100 and 800 mg $L^{-1}$. This systematic approach enabled a detailed analysis of the adsorption behavior of amoxicillin and metronidazole on AC-CSh. The yield and the quantity of antibiotics adsorbed were calculated using Formulas (1) and (2), providing valuable insights into the adsorption process.

$$q_e = (C_0 - C_e) \times \frac{V}{m} \tag{1}$$

$$R\% = 100 - \frac{100 \times C_e}{C_0} \tag{2}$$

where $C$ is concentration in (mg $L^{-1}$). V is the volume in (L), m is mass of activated carbon in (g), and R% is yield removal.

## 3 Results and Discussion

### *3.1 Study of Biochar Synthesis Parameters*

To optimize the synthesis parameters of biochar derived from *Cistus ladaniferus* shells and seeds, the effects of temperature, particle size, and heating rate on biochar yield were investigated. The results are presented in Fig. 2. Fig. 2a shows that as the temperature increases from 200°C to 450°C, the biochar yield decreases significantly. At lower temperatures (<300°C), thermal degradation is minimal, resulting in a higher biochar yield. However, at higher temperatures, volatile components of the biomass such as cellulose, hemicellulose, and lignin, decompose, leading to increased production of gas and bio-oil at the expense of biochar. Additionally, higher heating rates (21°C $min^{-1}$) accelerate this decomposition process, further reducing the biochar yield, particularly at elevated temperatures. Fig. 2d confirms that biochar yield consistently declines with increasing temperature (200°C–550°C), regardless of the heating rate. At lower heating rates (20°C $min^{-1}$), pyrolysis proceeds more slowly, favoring the preservation of carbonaceous materials. In contrast, higher heating rates (60–70°C $min^{-1}$) enhance thermal degradation, leading to a more rapid decrease in biochar yield. Fig. 2b highlights the direct impact of heating rate on biochar yield. At lower heating rates (7–14°C $min^{-1}$), pyrolysis occurs more gradually, allowing for better preservation of the biochar. However, at heating rates above 21°C $min^{-1}$, the yield stabilizes or slightly increases potentially due to incomplete pyrolysis at very high rates, which prevents full decomposition of volatile compounds. Fig. 2e reinforces these findings. At constant temperatures, lower heating rates (<40°C $min^{-1}$) result in slow and efficient conversion, maintaining a higher biochar yield. Conversely, at higher heating rates (>60°C $min^{-1}$), the yield stabilizes, likely due to partial pyrolysis that limits the complete release of volatile compounds.

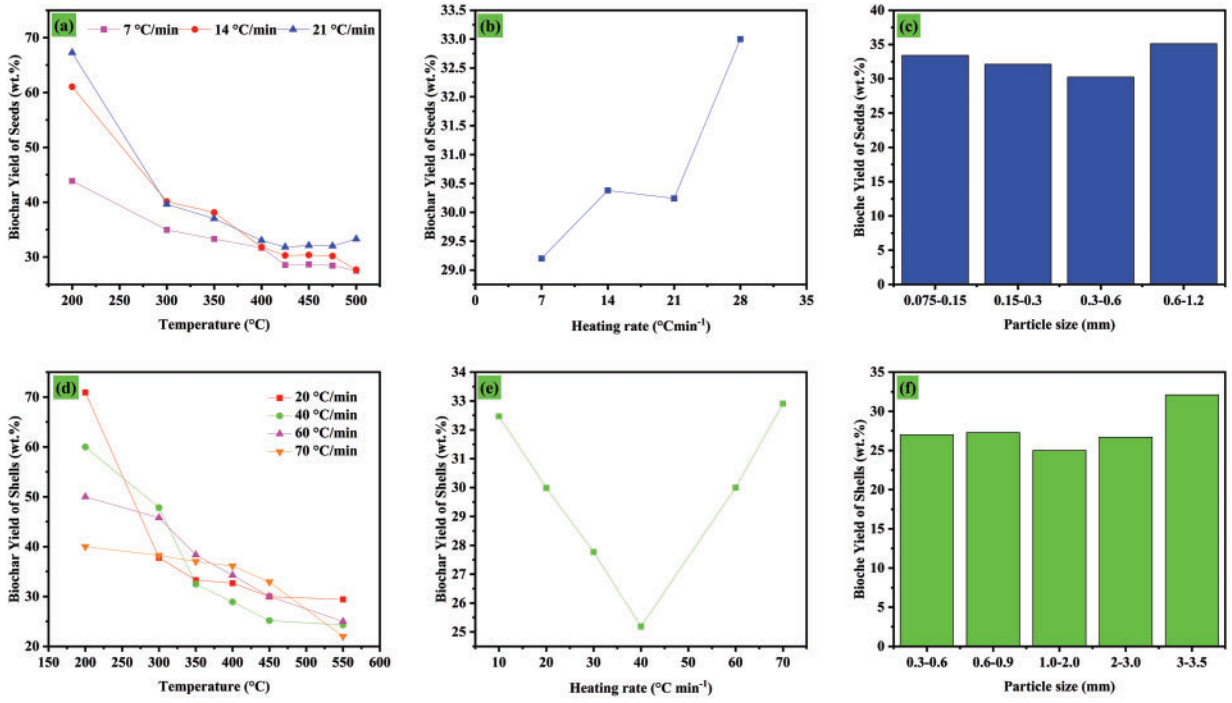


**Figure 2:** Influence des parameters of pyrolysis process on temperature (a) seeds, (d) shells, heating rate (b) seeds, (e) shells and particle size (c) seeds, (f) shells on yield of biochar

Fig. 2c,f explores the influence of biomass particle size on biochar yield for seeds and shells, respectively. In Fig. 2c, smaller seed particles (0.075–0.5 mm) produce a slightly lower biochar yield compared to larger seed particles (0.6–1.2 mm). This is likely due to the faster and more uniform thermal diffusion in smaller particles, which promotes more complete pyrolysis and a higher release of volatile compounds. In contrast, larger seed particles experience less complete pyrolysis because of their lower specific surface area and limited thermal diffusion, resulting in a higher biochar retention. A similar pattern is observed in Fig. 2f for shell particles ranging from 0.3 to 3.5 mm. Larger shell particles (3–3.5 mm) retain more biochar, as their bulkier structure limits the extent of thermal degradation. These findings underscore the significant role of particle size in optimizing biochar production for different types of biomasses.

### *3.2 Biochar and Activted Carbon Analysis*

#### *3.2.1 FTIR Analysis*

The FTIR spectrum presented in Fig. 3a and Table 1 highlights several key functional groups. Low-intensity vinyl C=C-H bonds are detected between 2925 and 3100 $cm^{-1}$, while conjugated and non-conjugated nitrile C≡N bonds appear between 2230 and 2250 $cm^{-1}$. The spectrum also reveals the emergence of aliphatic N-O bands within the 1380–1540 $cm^{-1}$ range and carboxylic acid C-O bonds between 1250 and 1300 $cm^{-1}$. Additionally, substituted alkene C-H bonds are identified in the 800–990 $cm^{-1}$ range. In Fig. 3b and Table 1, the FTIR spectrum exhibits the formation of new functional groups. N-H amine bonds with low to medium intensity appear between 3400 and 3500 $cm^{-1}$, alongside O-H stretching vibrations within the from 3200 to 3400 $cm^{-1}$ range. The low-intensity features between 2300 and 2500 $cm^{-1}$, attributed to salt ions such as $Cl^-$, $Na^+$, and $CO_3^{2-}$ in trace concentrations. The Carbonyl C=O bonds of aldehydes and ketones are present between 1685 and 1720 $cm^{-1}$, aromatic C-O bonds are observed from 1220 to 1260 $cm^{-1}$, and C-S bonds display high intensity at 1250 $cm^{-1}$. Additionally, benzene C-H bonds are evident beetwen 500 and 690 $cm^{-1}$ range.

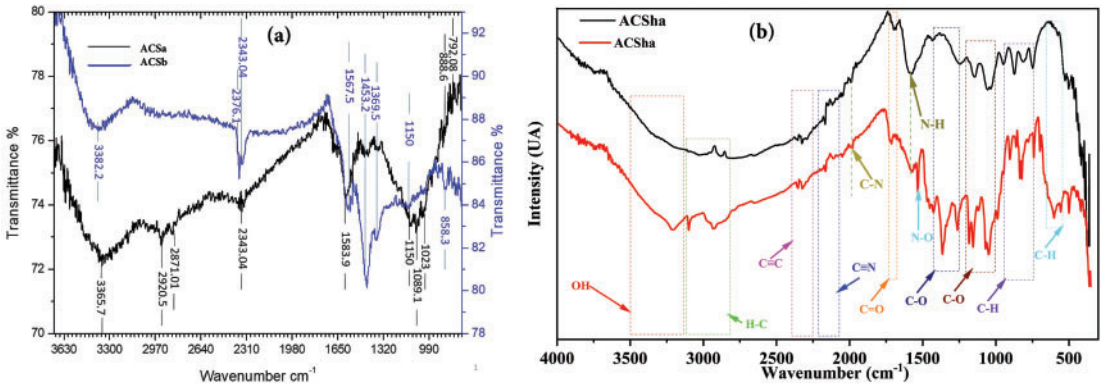


**Figure 3:** FTIR of activated carbon from cistus seeds ACS (a) and activated carbon from cistus shells ACSh (b)

**Table 1:** FTIR analysis of ACS and ACSh

| Functional group | Wavenumber range ($cm^{-1}$) |
|---|---|
| Vinyl C=C-H bonds | 2925–3100 |
| Nitrile C≡N bonds (conjugated & non-conjugated) | 2230–2250 |
| Aliphatic N-O bands | 1380–1540 |

(Continued)

**Table 1 (continued)**

| Functional group | Wavenumber range ($cm^{-1}$) |
|---|---|
| Carboxylic acid C-O bonds | 1250–1300 |
| Substituted alkene C-H bonds | 800–990 |
| N-H amine bonds (low to medium intensity) | 3400–3500 |
| O-H stretching vibrations | 3200–3400 |
| Salt ions ($Cl^-$, $Na^+$, $CO_3^{2-}$) | 2300–2500 |
| Carbonyl C=O bonds (aldehydes, ketones) | 1685–1720 |
| Aromatic C-O bonds | 1220–1260 |
| C-S bonds | 1250 |
| Benzene C-H bonds | 500–690 |

### *3.2.2 Brunauer-Emmet-Teller (BET) Analysis*

The nitrogen adsorption-desorption isotherms demonstrated a type IV pattern, characteristic of mesoporous materials. As shown in Figs. 4b and 5a, the isotherm could be divided into three distinct stages: (1) an initial phase ($p/p_0 < 0.48$), corresponding to monolayer adsorption of nitrogen on the walls of the mesopores; (2) a middle phase ($0.48 < p/p_0 < 1.05$), dominated by capillary condensation within the mesopores, where the inflection point indicative the mesopore diameter and a sharp transition suggests a narrow pore size distribution; and (3) a final plateau ($p/p_0 > 1.05$), associated with multilayer adsorption on the external surfaces of particle. Similar behavior has been reported in materials such as silica, green algae, coconut shell charcoal, and natural diatomite [15,19,20]. The specific surface area ($A_{BET}$) of ACSa, calculated using the BET method, was 678.74 $m^2\ g^{-1}$, with a pore volume of 0.9 $cm^3$ and an average pore diameter of 2.73 nm [15]. Furthermore, the BJH model estimated an average pore size of approximately 3.1 nm, as illustrated in Fig. 5b. Similarly, the adsorption properties of ACSha revealed a type IV isotherm profile (Fig. 4b), with three distinct phases: (1) initial adsorption of nitrogen onto the mesopore walls ($p/p_0 < 0.404$); (2) a notable increase in adsorption ($0.404 < p/p_0 < 0.99$), attributed to capillary condensation and the insertion of nitrogen molecule within the pores; and (3) a final plateau ($p/p_0 \approx 0.99$), reflecting multilayer adsorption on the external surface of particles. ACSha exhibited a higher specific surface area ($A_{BET}$) of 1210 $m^2\ g^{-1}$, with a pore volume of 0.75 $cm^3$, and an average pore diameter of 2.73 nm. The BJH analysis showed an average pore size of 3.732 nm, as illustrated in Fig. 4a.

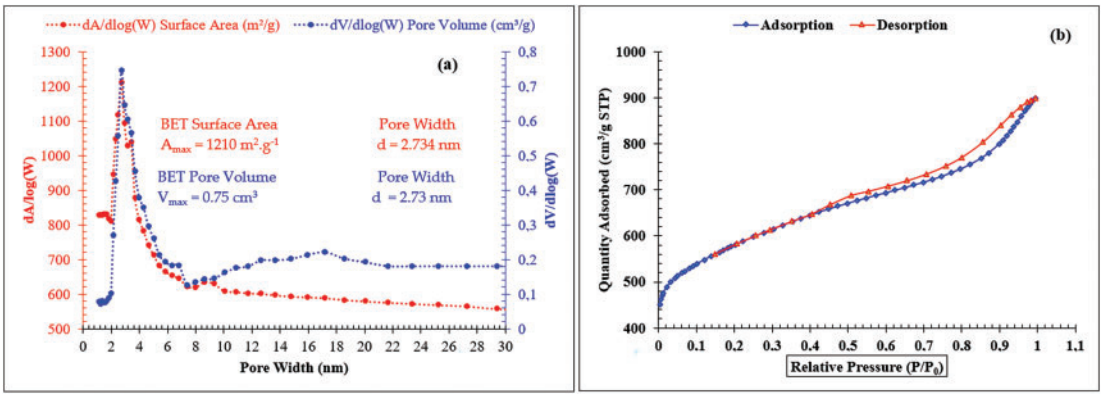


**Figure 4:** (a) dA/dlog(W) surface area, dV/dlog(W) pore volume, (b) Adsorption-desorption isotherm of ACSha

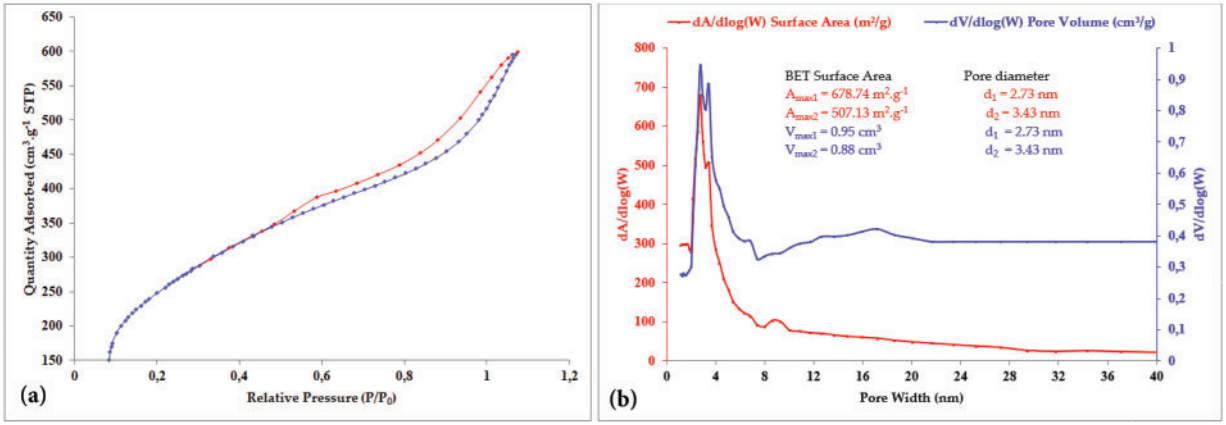


**Figure 5:** (a) Adsorption-desorption isotherm, (b) dA/dlog(W) surface area, dV/dlog(W) pore volume of ACSa

### *3.2.3 SEM and EDXA Analysis*

The biochar activation process, whether using NaOH as a base or $H_3PO_4$ as an acid, plays a critical role in developing biochar porosity. Charcoal synthesized from acid-activated cistus seeds (Fig. 6b,e) exhibits a stable porous structure, in contrast to the less porous structure of charcoal activated using a base (ACSb, ACShb, Fig. 6c,f). A similar trend is observed for charcoal obtained from acid-activated shells. Notably, the charcoal synthesized from shells demonstrates a more porous sheet like structure, which results in a higher specific surface area as measured by the BET method compared to that of charcoal derived from seeds. Carbon content analysis through EDXA reveals that acid-activated biochars possess a higher carbon percentage compared to base-activated biochars (ACSa, ACSha, Fig. 7) for both types of charcoal. The enhanced porosity and increased carbon content in acid-activated biochars contribute to their superior adsorption properties, making them highly effective in wastewater treatment applications.

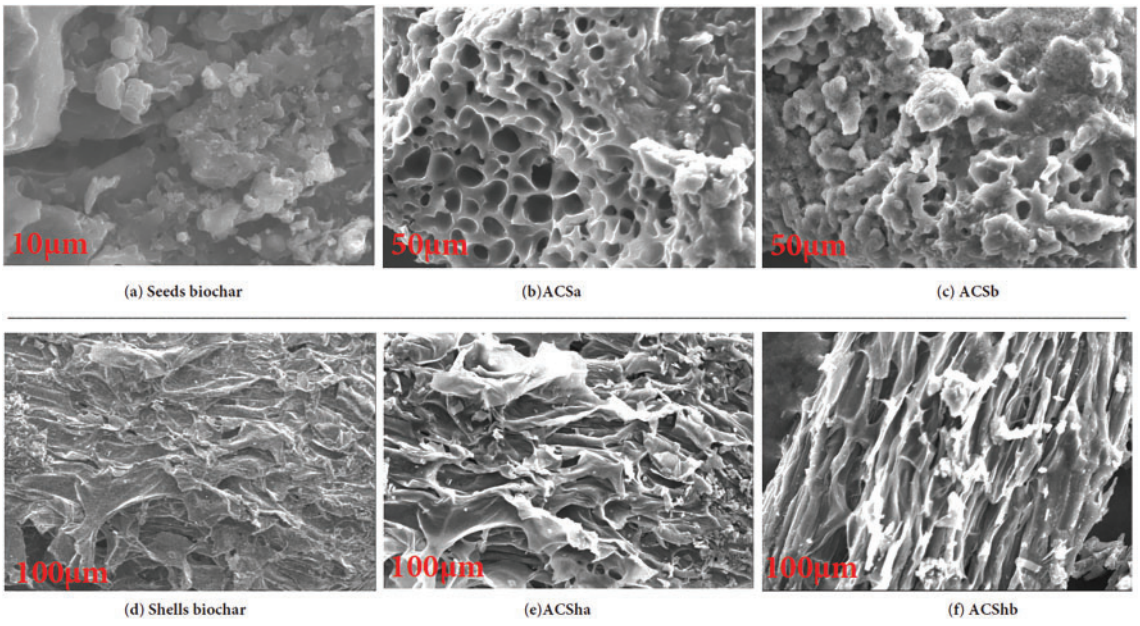


**Figure 6:** SEM micrographs

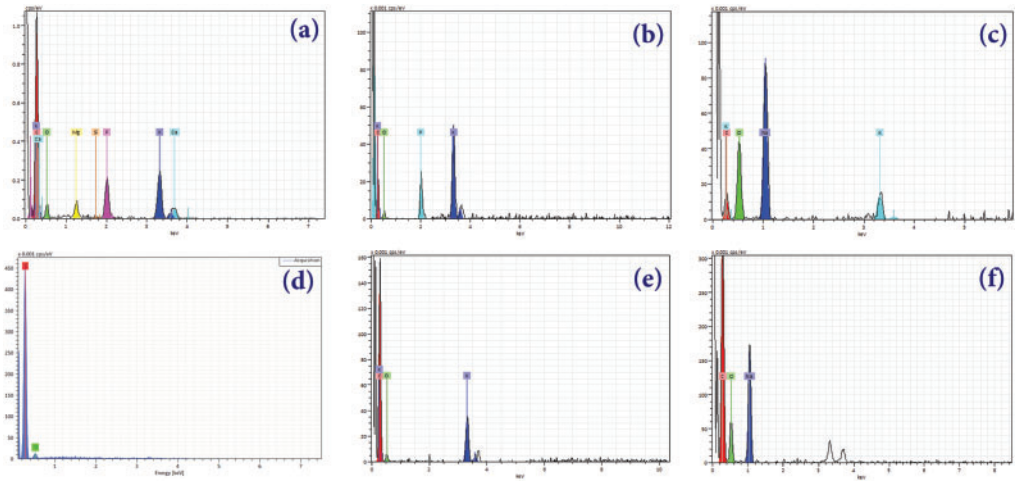


**Figure 7:** EDXA diffractograms (a) Seeds biochar, (b) ACSa, (c) ACSb, (d) Shells biochar, (e) ACSha and (f) ASChb

Activated carbon is widely recognized for its excellent adsorption capacity, which is critical for the removal of contaminants from wastewater. Chemical activation, a key step in its production, involves impregnating carbon-rich materials (e.g., coconut shells, wood, coal) with activating agents such as potassium hydroxide (KOH), phosphoric acid ($H_3PO_4$), or zinc chloride ($ZnCl_2$). This activation process significantly enhances the porosity and surface area of the material, thereby improving its adsorption efficiency. For instance, Soliman et al. [21] reported that chemical activation using a combination of hydrochloric acid (HCl) and hydrogen peroxide ($H_2O_2$) enabled the preparation of highly efficient adsorbents from sludge, achieving a 99.9% removal efficiency in wastewater treatment. Additionally, persulfate (PS) activation has attracted significant attention for its effectiveness in degrading recalcitrant contaminants. Chemical activation methods, including the use of transition metals or alkaline conditions, are employed to activate persulfate, producing sulfate radicals ($SO_4^{2-}$), which are potent oxidants capable of degrading a wide range of pollutants. Recent research, as reviewed by Wang et al. [22], highlights various chemical activation strategies developed to enhance the efficiency of PS activation in wastewater treatment applications.

Table 2 highlights the elemental composition of biochars and their activated carbon derivatives derived from seeds and shells. Carbon content is high across all samples, with ACSha exhibiting the highest percentage (96.40 wt.%), indicating that the activation process effectively enhances carbon concentration. Simultaneously, oxygen levels decrease significantly in the activated carbons, with ACSha recording the lowest value (2.37 wt.%), suggesting the removal of oxygenated functional groups during activation. Potassium is present in small amounts, with seeds biochar showing the highest concentration (1.34 wt.%). Trace elements such as calcium, magnesium, and silicon are only detected in seeds biochar and are entirely removed during activation process. Phosphorus remains relatively stable in the activated carbons derived from seeds, with ACSa and ACSha showing 1.47 wt.% and 1.01 wt.%, respectively. Sodium is notably concentrated in ACSb (13.04 wt.%), likely due to the activation process or residual salts. These variations in elemental composition reflect the impact of activation on biochars, enhancing their properties and making them more suitable for applications like adsorption or catalysis. Overall, the concentrations of metals in the biomass are low, typically not exceeding 0.1%, except for certain elements such as manganese. Non-metallic elements, including phosphorus (P), calcium (Ca), sulfur (S), and potassium (K) also have concentrations below 1%. This composition indicates that the biomass is rich in carbon and oxygen, a favorable characteristic for utilizing cistus seeds and shells as a potential source of biofuels.

**Table 2:** Elements identified by EDXA in seeds biochar, ACSa, ACSb, shells biochar, ACSha and ASChb

| Elements | Seeds biochar | ACSa | ACSb | Shells biochar | ACSha | ASChb |
|---|---|---|---|---|---|---|
| | wt.% | | | | | |
| Carbone | 85.43 | 90.13 | 50.72 | 95.18 | 96.40 | 91.10 |
| Oxygène | 11.07 | 7.22 | 36.11 | 4.82 | 2.37 | 7.17 |
| Potassium | 1.34 | 1.18 | 0.13 | nd | 0.22 | nd |
| Calcium | 0.36 | nd | nd | nd | nd | nd |
| Phosphore | 0.97 | 1.47 | nd | nd | 1.01 | nd |
| Magnésium | 0.77 | nd | nd | nd | nd | nd |
| Silicium | 0.06 | nd | nd | nd | nd | nd |
| Sodium | nd | nd | 13.04 | nd | nd | 1.74 |

Note: nd: not determined.

Elemental analysis (CHNSO), a widely used and reliable technique based on sample combustion, was conducted using the Micro TruSpec instrument (EA3000). This instrument simultaneously measures the contents of carbon (C), hydrogen (H), nitrogen (N), and sulfur (S), while oxygen (O) is analyzed separately through a pyrolysis process. Table 3 presents the results of this analysis along with the characteristics of biochar and activated carbon.

**Table 3:** Ultimate analysis and property of seeds biochar, ACSa, ACSb, shells biochar, ACSha and ASChb

| Property/element | Seeds biochar (wt.%) | ACSa (wt.%) | ACSb (wt.%) | Shells biochar (wt.%) | ACSha (wt.%) | ASChb (wt.%) |
|---|---|---|---|---|---|---|
| Carbon | 82.34 | 89.17 | 66.98 | 87.02 | 92.48 | 90.19 |
| Oxygen | 14.25 | 9.09 | 30.03 | 8.92 | 5.37 | 7.01 |
| Hydrogen | 2.33 | 1.44 | 2.78 | 2.94 | 1.53 | 1.83 |
| Nitrogen | 0.93 | 0.30 | 0.21 | 1.01 | 0.62 | 0.97 |
| Sulfur | 0.15 | nd | nd | 0.11 | nd | nd |
| Moisture (%) | 4.12 | 2.37 | 2.82 | 3.96 | 1.98 | 1.13 |
| pH | 8.85 | 6.85 | 8.52 | 8.10 | 7.14 | 9.02 |
| Conductivity (µS/cm) | 425 | 720 | 1185 | 515 | 898 | 1395 |

Table 3 provides a clear comparison of the properties of biochar and activated carbon derived from seeds and shells. Activated carbons exhibit significantly higher carbon content (e.g., 92.48% for ACSha and 89.17% for ACSa) compared to biochars (82.34% for seeds and 87.02% for shells), reflecting their enhanced stability and superior adsorption capabilities. In contrast, Biochars, contain a higher oxygen content (14.25% for seeds and 8.92% for shells), indicating the presence of oxygen-based functional groups. The activation process substantially reduces this oxygen content significantly (e.g., 5.37% for ACSha), thereby increasing hydrophobicity and enhancing material durability. Hydrogen levels are slightly higher in biochars, suggesting that the devolatilization process during pyrolysis is less complete compared to activated carbons. Nitrogen content is relatively low across all samples but slightly higher in shell-based samples, likely due to the composition of the raw feedstock. Additionally, Sulfur is nearly absent in activated carbons, a beneficial characteristic that helps minimize environmental impact.

Moisture content is significantly lower in activated carbons (e.g., 1.98% for ACSha), reflecting their higher porosity and hydrophobic nature. Biochars, on the other hand, exhibit an alkaline pH (e.g., 8.85 for seeds), making them particularly suitable for applications like soil improvement, In contrast, activated carbons display greater variation in pH, depending on the activation process employed. Additionally, electrical conductivity is markedly higher in activated carbons (e.g., 1395 µS/cm for ASChb), indicating a greater capacity for ion exchange and higher mineral content. These findings highlight the superior properties of activated carbons, making them more effective for applications such as adsorption and environmental remediation.

### *3.2.4 XRD Analysis*

The X-ray diffractograms (Fig. 8) of samples ACSha, ACShb, ACSa, and ACSb highlight notable differences based on the chemical activation method used ($H_3PO_4$ or NaOH). ACSHa and ACSa, activated with $H_3PO_4$, exhibit broad, low intensity peaks around $2\theta$ range of 20°–30°, indicative of amorphous or weakly crystalline structures. This pattern is typical of activated carbons that have undergone limited chemical activation or insufficient heat treatment. In contrast, ACShb and ACSb, activated with NaOH, demonstrate significantly higher crystallinity. ACShb displays well defined peaks, particularly at $2\theta° \approx 26°$ (graphite (002) plane), as well as at 24°, 33°, and 49° ($Fe_2O_3$), and 42°–43° (MgO), indicating atomic reorganization facilitated by NaOH activation. Similarly, ACSb shows sharp peaks at $2\theta° \approx 26°$ (graphite), 43° and 50° ($Fe_3O_4$ or $TiO_2$), and 33° and 62° ($Fe_2O_3$), reflecting high crystalline structure resulting from high temperature chemical impregnation and pyrolysis. Thus, NaOH-activated samples (ACShb and ACSb) exhibit prominent crystalline features, whereas $H_3PO_4$-activated samples (ACSha and ACSa) retain predominantly amorphous characteristics.

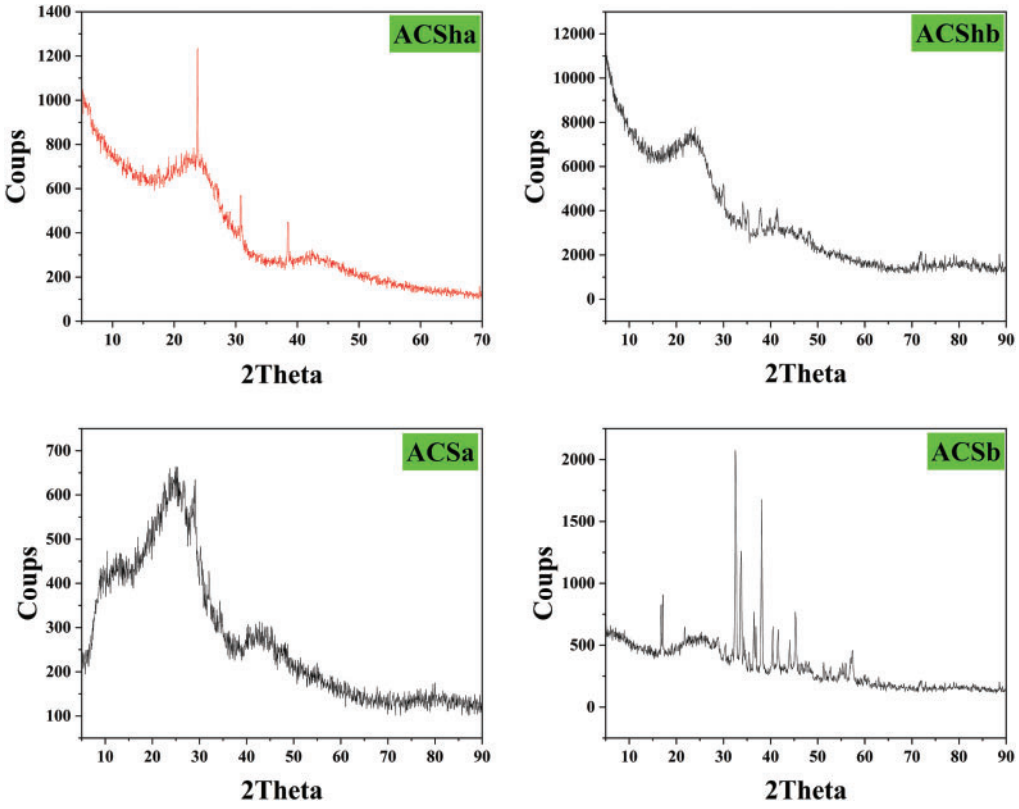


**Figure 8:** X-ray diffractograms

### *3.3 Application in Adsorption*

Activated carbons derived from citus ladaniferus seeds and shells (ACS and ACSh), chemically activated with phosphoric acid ($H_3PO_4$), offer an efficient solution for the adsorption of azo dyes and heavy metals. Their microporous structure and oxygenated functional groups facilitates strong interactions with these pollutants through mechanisms such as ion exchange, $\pi$-$\pi$ interactions, and complexation. These materials demonstrate significant potential for wastewater treatment, effectively combining sustainability with the valorization of agricultural residues.

#### *3.3.1 Kinetics Adsorption*

Table 4 presents detailed kinetic parameters for various adsorption experiments, evaluating the performance of different adsorbents (BS, BSh, ACSha, ACSa) with several adsorbates (dyes, antibiotics, and metal ions) using pseudo-first-order, pseudo-second-order, and intraparticle diffusion models. Across most cases, pseudo-second-order kinetics model provides the best fit with $R^2$ values approaching 1, indicating that adsorption is primarily governed by chemical interactions. For instance, ACSha demonstrates an excellent fit for Amoxicillin ($R^2$ = 0.954) and Metronidazole ($R^2$ = 0.929). Similarly. BS adheres strongly to the second-order model for RR23 ($R^2$ = 0.998) and AO52 ($R^2$ = 0.998), while BSh exhibits comparable behavior for RR23 ($R^2$ = 0.999) and AO52 ($R^2$ = 0.998) [23,24]. The pseudo-first-order model shows slightly weaker fits, but still performs adequately in some cases such as AO52 adsorption on BS ($R^2$ = 0.896) and $Ni^{2+}$ on ACSa ($R^2$ = 0.874). For the intraparticle diffusion model, the $R^2$ values for ACSha with Amoxicillin ($R^2$ = 0.881) and BS with AO52 ($R^2$ = 0.932) suggest that diffusion plays a significant role. However, other combinations, such as ACSa with $Cu^{2+}$ ($R^2$ = 0.701) and BSh with RR23 ($R^2$ = 0.553), indicate weaker fits, suggesting that intraparticle diffusion is not the dominant mechanism in these cases. Adsorption capacities ($Q_e$) vary widely, with ACSha achieving the highest values for Amoxicillin (237.68 mg $g^{-1}$) and Metronidazole (207.07 mg $g^{-1}$). ACSa shows strong adsorption performance for $Ni^{2+}$ (79.64 mg $g^{-1}$) and $Cr^{6+}$ (99.84 mg $g^{-1}$), accompanied by relatively high $K_2$ values (e.g., $Ni^{2+}$: $0.7 \times 10^{-3}$ g $mg^{-1}$ min, $Cr^{6+}$: $0.8 \times 10^{-3}$ g $mg^{-1}$ min) [15,25,26].

**Table 4:** Kinetics models parameters

| Kinetics models | | Pseudo first order | | | | Pseudo second order | | | | Intraparticle diffusion | | |
|---|---|---|---|---|---|---|---|---|---|---|---|---|
| **Adsorbent** | **Adsorbate** | $Q_e$ | $Q_{cal}$ | $K_1$ | $R^2$ | $Q_e$ | $Q_{cal}$ | $K_2$ | $R^2$ | $K_i$ | C | $R^2$ |
| BS | RR23 | 43.81 | 25.23 | 0.08 | 0.998 | 43.81 | 47.62 | $4.9 \times 10^{-3}$ | 0.998 | 1.65 | 28.73 | 0.565 |
| | AO52 | 130.23 | 256.47 | 0.06 | 0.896 | 130.23 | 166.67 | $2.8 \times 10^{-3}$ | 0.998 | 9.85 | 35.44 | 0.932 |
| BSh | RR23 | 49.75 | 10.06 | 0.06 | 0.999 | 49.75 | 52.63 | $7.0 \times 10^{-3}$ | 0.999 | 1.42 | 36.71 | 0.553 |
| | AO53 | 190.77 | 227.47 | 0.06 | 0.908 | 190.77 | 250.00 | $0.4 \times 10^{-3}$ | 0.998 | 9.26 | 102.00 | 0.880 |
| ACSha | Amoxicillin | 237.68 | 544.68 | 0.06 | 0.954 | 237.68 | 263.16 | $0.3 \times 10^{-3}$ | 0.998 | 9.60 | 129.44 | 0.881 |
| | Metronidazole | 207.07 | 904.05 | 0.10 | 0.929 | 207.07 | 217.39 | $0.8 \times 10^{-3}$ | 0.999 | 5.35 | 149.63 | 0.725 |
| ACSa | RR23 | 80.40 | 382.98 | 0.11 | 0.885 | 333.33 | 382.98 | $0.7 \times 10^{-3}$ | 0.996 | 10.08 | 192.30 | 0.585 |
| | $Cu^{2+}$ | 93.90 | 155.87 | 0.09 | 0.935 | 93.90 | 103.10 | $0.8 \times 10^{-3}$ | 0.9984 | 4.57 | 46.85 | 0.701 |
| | $Ni^{2+}$ | 79.64 | 154.47 | 0.068 | 0.874 | 79.64 | 89.29 | $0.7 \times 10^{-3}$ | 0.9963 | 4.50 | 32.73 | 0.818 |
| | $Cr^{6+}$ | 99.84 | 179.11 | 0.084 | 0.888 | 99.84 | 112.36 | $0.8 \times 10^{-3}$ | 0.9972 | 4.74 | 51.46 | 0.643 |

Note: BS: biochar seeds, BSh: biochar shells, ACSa: activated carbon of seeds by acid, ACSha: activated carbon of shells by acid, RR23: read reactif 23, AO52: acid orange 52, $R^2$: correlation coefficient; $Q_e$ (mg $g^{-1}$): quantity of adsorbed at equilibrium; $K_1$ (mL $min^{-1}$): first order adsorption rate constant; $K_2$ (g $mg^{-1}$ $min^{-1}$): second order adsorption rate constant; $K_i$ (mg · $g^{-1}$ $min^{-0.5}$) is the intraparticle diffusion rate constant. The value of the y-intercept C (mg $g^{-1}$).

### *3.3.2 Isotherms Adsorption*

The Table 5 summarizes the adsorption performance of various adsorbents (ACSa, ACSha, BS, and BSh) for different adsorbates evaluated using Langmuir and Freundlich isotherm models. ACSa demonstrates high adsorption capacities for $Cu^{2+}$ (238.10 g $mg^{-1}$), $Ni^{2+}$ (80.64 g $mg^{-1}$), and $Cr^{6+}$ (125 g $mg^{-1}$) [15], with Langmuir $R^2$ values exceeding 0.995, indicating an excellent fit to the model. ACSha exhibits exceptional adsorption capacities for amoxicillin (1250 g $mg^{-1}$) and metronidazole (769.23 g $mg^{-1}$), with Freundlich *n* values close to 1, suggesting favorable adsorption under these conditions. BS and BSh show significant adsorption capacities for dyes, such as RR23 (166.67 and 354.82 g $mg^{-1}$, respectively) [27], and AO52 (333.33 and 500 g $mg^{-1}$, respectively). The higher $R^2$ values for the Langmuir model suggest that monolayer adsorption dominates, while Freundlich parameters (e.g., $n$ = 2.739 for BSh) indicate heterogeneous adsorption adsorption process for some materials. These findings underscore the effectiveness of the studied adsorbents in removing heavy metals, antibiotics, and dyes from aqueous solutions, with BSh standing out as the material with the highest adsorption capacity.

**Table 5:** Isotherms models parameters

| Models | | Langmuir isotherm | | | | Freundlich isotherm | | |
|---|---|---|---|---|---|---|---|---|
| **Adsorbent** | **Adsorbate** | **$R_L$** | **$K_L$ (L $mg^{-1}$)** | **$Q_{e,m}$ (mg $g^{-1}$)** | **$R^2$** | **$K_F$** | ***n*** | **$R^2$** |
| ACSa | $Cu^{2+}$ | 0.4842–0.8492 | 0.0071 | 238.10 | 0.9958 | 0.1814 | 11.399 | 0.970 |
| | $Ni^{2+}$ | 0.1218–0.4545 | 0.0480 | 80.64 | 0.9968 | 0.7416 | 20.399 | 0.980 |
| | $Cr^{6+}$ | 0.4425–0.8264 | 0.0084 | 125 | 0.9965 | 0.9985 | 20.610 | 0.992 |
| ACSha | Amoxicillin | 0.17–0.62 | 0.0061 | 1250 | 0.9971 | 11.98 | 1.25 | 0.9982 |
| | Metronidazole | 0.13–0.55 | 0.0082 | 769.23 | 0.9905 | 9.94 | 1.26 | 0.9867 |
| BS | RR23 | 0.0680–0.4219 | 0.175 | 166.67 | 0.996 | 20.267 | 1.408 | 0.989 |
| | AO52 | 0.0694–0.4273 | 0.0268 | 333.333 | 0.988 | 21.867 | 1.972 | 0.899 |
| BSh | RR23 | 0.0174–0.1508 | 0.563 | 354.82 | 0.984 | 57.054 | 2.283 | 0.984 |
| | AO52 | 0.0132–0.1182 | 0.1492 | 500 | 0.993 | 44.523 | 2.739 | 0.965 |

## 4 Conclusion

Activated carbons derived from Cistus ladaniferus seeds and shells were synthesized through pyrolysis, followed by chemical activation using phosphoric acid ($H_3PO_4$) or base sodium hydroxide NaOH. The pyrolysis process converts biomass into biochar under controlled conditions, increasing its carbon content while reducing volatile matter. Subsequent activation with $H_3PO_4$ creates a highly microporous structure and introduces oxygenated functional groups, which are crucial for effective adsorption performance. Comprehensive characterization of these materials confirmed their enhanced properties, including BET surface area analysis, pore size distribution, and functional group identification. These findings highlight the materials' potential for various environmental applications, particularly in the adsorption of pollutants.

The activated carbons exhibit exceptional adsorption capacities for a wide range of pollutants, including azo dyes, heavy metals, and pharmaceuticals, due to their tailored porosity and surface chemistry. Adsorption kinetics predominantly follow the pseudo-second-order model, underscoring the dominance of chemisorption. For example, ACSha demonstrates remarkable adsorption capacities for amoxicillin ($Q_e$ = 237.68 mg $g^{-1}$, $R^2$ = 0.998) and metronidazole ($Q_e$ = 207.07 mg $g^{-1}$, $R^2$ = 0.999). Similarly, ACSa efficiently adsorbs heavy metals such as $Cr^{6+}$ ($Q_e$ = 99.84 mg $g^{-1}$, $R^2$ = 0.9972) and $Cu^{2+}$ ($Q_e$ = 93.90 mg $g^{-1}$, $R^2$ = 0.9984). Adsorption

isotherm analysis reveals that the Langmuir model provides an excellent fit for most cases, indicating monolayer adsorption. ACSa exhibits high maximum adsorption capacities ($Q_{e,m}$) for $Cu^{2+}$ (238.10 mg $g^{-1}$), $Ni^{2+}$ (80.64 mg $g^{-1}$), and $Cr^{6+}$ (125 mg $g^{-1}$), with $R^2$ values exceeding 0.995. In pharmaceutical adsorption, ACSha achieves outstanding results, with capacities of 1250 mg $g^{-1}$ for amoxicillin and 769.23 mg $g^{-1}$ for metronidazole. Additionally, the Freundlich model highlights the heterogeneous adsorption behavior, of some materials, such as BSh for AO52 ($n$ = 2.739).

This study underscores the dual benefits of biochar and activated carbon synthesis: the valorization of agricultural residues and development of efficient adsorbents for environmental remediation. The synergy between pyrolysis and chemical activation yields materials with superior adsorption properties, making them highly effective for addressing wastewater treatment challenges. Future research should focus on optimizing production processes, investigating regeneration potential, and scaling up these materials for industrial applications.

**Acknowledgement:** This work is part of the efforts to valorize bioresources within the Laboratory of Environment and Applied Chemistry (LCAE) at Mohammed First University, Oujda, and the Chemical Engineering for Resources Valorization Group (UAE/L01FST) at the Faculty of Science and Technology, Abdelmalek Essaadi University, Tangier, Morocco. The authors express their sincere gratitude to the Director of the Analysis Platform at the Faculty of Sciences in Oujda for kindly providing access to the necessary facilities and materials.

**Funding Statement:** The authors received no specific funding for this study.

**Author Contributions:** The authors confirm contribution to the paper as follows: Conceptualization, Hammadi El Farissi, Anass Choukoud and Bouchaib Manoun; methodology, Hammadi El Farissi and Bouchaib Manoun; software, Hammadi El Farissi; validation, Hammadi El Farissi, Bouchaib Manoun and Mohamed El Massaoudi ; formal analysis, Hammadi El Farissi and Bouchaib Manoun; investigation, Hammadi El Farissi, Anass Choukoud and Bouchaib Manoun; data curation, Hammadi El Farissi; writing—original draft preparation, Hammadi El Farissi, Anass Choukoud and Bouchaib Manoun; writing—review and editing, Hammadi El Farissi, Bouchaib Manoun, Mohamed El Massaoudi and Abdelmonaem Talhaoui; supervision, Hammadi El Farissi. All authors reviewed the results and approved the final version of the manuscript.

**Availability of Data and Materials:** Data available within the article.

**Ethics Approval:** Not applicable.

**Conflicts of Interest:** The authors declare no conflicts of interest to report regarding the present study.

## References

1. Wang L, Wang L, Li Y, Wang J. A century-long analysis of global warming and earth temperature using a random walk with drift approach. Decis Anal J. 2023;7(251):100237. doi:10.1016/j.dajour.2023.100237.
2. Intergovernmental Panel on Climate Change (IPCC). Health, wellbeing and the changing structure of communities. In: Climate change 2022—impacts, adapt and vulnerability. Cambridge, UK: Cambridge University Press; 2023. p. 1041–170. doi:10.1017/9781009325844.009.
3. Pörtner H-O, Roberts DC, Tignor MMB, Poloczanska E, Mintenbeck K, Alegría A, et al. Climate change 2022—impacts, adaptation and vulnerability—working group ii contribution to the sixth assessment report of the intergovernamental panel on climate change. Cambridge, UK: Cambridge University Press; 2022. 37 p. doi:10.1017/9781009325844.
4. Birch EL. A Review of climate change 2014: impacts, adaptation, and vulnerability and climate change 2014: mitigation of climate change. J Am Plan Assoc. 2014;80(2):184–5. doi:10.1080/01944363.2014.954464.

5. Roberts D, O'Donoghue S. Urban environmental challenges and climate change action in Durban, South Africa. Environ Urban. 2013;25(2):299–319. doi:10.1177/0956247813500904.
6. Afshar M, Mofatteh S. Biochar for a sustainable future: environmentally friendly production and diverse applications. Results Eng. 2024;23(8):102433. doi:10.1016/j.rineng.2024.102433.
7. Just C, Armbruster M, Barkusky D, Baumecker M, Diepolder M, Döring TF, et al. Soil organic carbon sequestration in agricultural long-term field experiments as derived from particulate and mineral-associated organic matter. Geoderma. 2023;434(1):116472. doi:10.1016/j.geoderma.2023.116472.
8. Anand A, Gautam S, Ram LC. Feedstock and pyrolysis conditions affect suitability of biochar for various sustainable energy and environmental applications. J Anal Appl Pyrolysis. 2023;170:105881. doi:10.1016/j.jaap.2023.105881.
9. Ginni G, Kavitha S, Yukesh Kannah R, Bhatia SK, Adish Kumar S, Rajkumar M, et al. Valorization of agricultural residues: Different biorefinery routes. J Environ Chem Eng. 2021;9(4):105435. doi:10.1016/j.jece.2021.105435.
10. Mergbi M, Galloni MG, Aboagye D, Elimian E, Su P, Ikram BM, et al. Valorization of lignocellulosic biomass into sustainable materials for adsorption and photocatalytic applications in water and air remediation. Environ Sci Pollut Res Int. 2023;30(30):74544–74. doi:10.1007/s11356-023-27484-2.
11. Anvari S, Aguado R, Jurado F, Fendri M, Zaier H, Larbi A, et al. Analysis of agricultural waste/byproduct biomass potential for bioenergy: the case of Tunisia. Energy Sustain Dev. 2024;78(S1):101367. doi:10.1016/j.esd.2023.101367.
12. Benali T, Laghmari M, Touhtouh J, Aanniz T, Lemhadri A, Daoudi MD, et al. Chemical composition and bioactivity of essential oils from *Cistus ladanifer* L., *Pistacia lentiscus* L., and *Matricaria chamomilla* L. Biochem Syst Ecol. 2024;116(1):104880. doi:10.1016/j.bse.2024.104880.
13. Amalina F, Razak ASA, Krishnan S, Sulaiman H, Zularisam AW, Nasrullah M. Biochar production techniques utilizing biomass waste-derived materials and environmental applications—a review. J Hazard Mater Adv. 2022;7(4):100134. doi:10.1016/j.hazadv.2022.100134.
14. El Farissi H, Beraich A, Lamsayah M, Talhaoui A, El Bachiri A. The efficiency of carbon modified by phosphoric acid ($H_3PO_4$) used in the removal of two antibiotics amoxicillin and metronidazole from polluted water: experimental and theoretical investigation. J Mol Liq. 2023;391(14):123237. doi:10.1016/j.molliq.2023.123237.
15. El Mansouri F, El Farissi H, Cacciola F, Talhaoui A, El Bachiri A, Tahani A, et al. Rapid elimination of copper (II), nickel (II) and chromium (VI) ions from aqueous solutions by charcoal modified with phosphoric acid used as a green biosorbent. Polym Adv Technol. 2022;33(7):2254–64. doi:10.1002/pat.5676.
16. Brunauer S, Emmett PH, Teller E. Adsorption of gases in multimolecular layers. J Am Chem Soc. 1938;60(2):309–19. doi:10.1021/ja01269a023.
17. Jorfi S, Darvishi Cheshmeh Soltani R, Ahmadi M, Khataee A, Safari M. Sono-assisted adsorption of a textile dye on milk vetch-derived charcoal supported by silica nanopowder. J Environ Manag. 2017;187:111–21. doi:10.1016/j.jenvman.2016.11.042.
18. Molina-Sabio M, Rodrı´guez-Reinoso F. Role of chemical activation in the development of carbon porosity. Colloids Surf A Physicochem Eng Aspects. 2004;241(1–3):15–25. doi:10.1016/j.colsurfa.2004.04.007.
19. Onay O. Influence of pyrolysis temperature and heating rate on the production of bio-oil and char from safflower seed by pyrolysis, using a well-swept fixed-bed reactor. Fuel Process Technol. 2007;88(5):523–31. doi:10.1016/j.fuproc.2007.01.001.
20. Ghaffari A, Tehrani MS, Husain SW, Anbia M, Azar PA. Adsorption of chlorophenols from aqueous solution over amino-modified ordered nanoporous silica materials. J Nanostruct Chem. 2014;4(3):114. doi:10.1007/s40097-014-0114-1.
21. Soliman MF, Rashed MN, Ali Ahmd A. Chemical activation of sludge from drinking water treatment plant for adsorption of methylene blue dye. Water Air Soil Pollut. 2023;234(4):228. doi:10.1007/s11270-023-06216-9.
22. Wang B, Wang Y. A comprehensive review on persulfate activation treatment of wastewater. Sci Total Environ. 2022;831(1):154906. doi:10.1016/j.scitotenv.2022.154906.
23. El Farissi H, Lakhmiri R, Albourine A, Safi M. The adsorption of the orange acid dye 52 in aqueous solutions by the biochar of the seeds and shells of Cistus Ladaniferus. Int J Sci Eng Res. 2018;9:563–71.

24. Yahia IS, Abd El-sadek MS, Yakuphanoglu F. Methyl orange (C.I. acid orange 52) as a new organic semiconductor: conduction mechanism and dielectrical relaxation. Dyes Pigm. 2012;93(1–3):1434–40. doi:10.1016/j.dyepig.2011.10.002.
25. Jin GP, Wang XL, Fu Y, Do Y. Preparation of tetraoxalyl ethylenediamine melamine resin grafted-carbon fibers for nano-nickel recovery from spent electroless nickel plating baths. Chem Eng J. 2012;203:440–6. doi:10.1016/j.cej.2012.07.055.
26. Shi T, Xie Z, Zhu Z, Shi W, Liu Y, Liu M. Highly efficient and selective adsorption of heavy metal ions by hydrazide-modified sodium alginate. Carbohydr Polym. 2022;276(7):118797. doi:10.1016/j.carbpol.2021.118797.
27. El Farissi H, Lakhmiri R, Albourine A, Safi M, Cherkaoui O. Adsorption study of charcoal of *Cistus* ladaniferus shell modified by $H_3PO_4$ and NaOH used as a low-cost adsorbent for the removal of toxic reactive red 23 dye: kinetics and thermodynamics. Mater Today Proc. 2021;43(4):1740–8. doi:10.1016/j.matpr.2020.10.438.